J. Fluid Mech. (2025), *vol.* 1024, A54, doi:10.1017/jfm.2025.10918

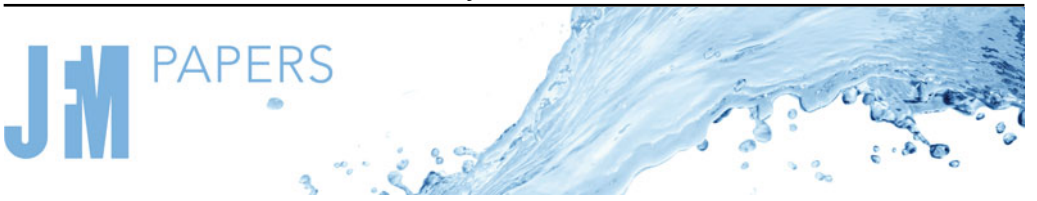

Axial oscillations of a sphere in a rotating cylinder

J. Rafael Pacheco[1,2], **Juan M. Lopez**[2] and **Roberto Verzicco**[3,4,5]

[1]Naval Air Warfare Center Aircraft Division NAWCAD, 22347 Cedar Point Road, Patuxent River, MD 20670, USA

[2]School of Mathematical and Statistical Sciences, Arizona State University, Tempe, AZ 85287-1804, USA

[3]Dipartimento di Ingegneria Meccanica, Universita' di Roma 'Tor Vergata', Via del Politecnico 1, Roma 00133, Italy

[4]PoF, University of Twente, Enschede 7500 AE, The Netherlands

[5]Gran Sasso Science Institute, Viale Rendina 26, L'Aquila 67100, Italy

Corresponding author: Juan M. Lopez; Email: juan.m.lopez@asu.edu

(Received 15 May 2025; revised 27 October 2025; accepted 2 November 2025)

The flow in a rapidly rotating cylinder forced by the harmonic oscillations of a small sphere along the rotation axis is explored numerically. For oscillation frequencies less than twice the cylinder rotation frequency, the forced response flows feature conical shear layers emitted from the critical latitudes of the sphere. These latitudes are where the characteristics of the hyperbolic system, arrived at by ignoring nonlinear, viscous and forcing terms in the governing equations, are tangential to the sphere. These conical shear layers vary continuously with the forcing frequency so long as it remains inertial. At certain values of the forcing frequency, linear inviscid inertial modes of the cylinder are resonated. Of all possible inertial modes, only those whose symmetries are compatible with the symmetry of the forced system are resonated. This all occurs even in the linear limit of vanishingly small forcing amplitude. As the forcing amplitude is increased, nonlinearity leads to non-harmonic oscillations and a non-zero mean flow which features a Taylor columnar structure extending from the sphere to the two endwalls in an axially invariant fashion.

Key words: waves in rotating fluids

1. Introduction

There has been, and continues to be, much interest in inertial waves due to their importance to oceanic, atmospheric, astrophysical and industrial flows. Inertial waves in the interior

© The Author(s), 2025. Published by Cambridge University Press. This is an Open Access article, distributed under the terms of the Creative Commons Attribution licence (https://creativecommons.org/licenses/by/4.0/), which permits unrestricted re-use, distribution and reproduction, provided the original article is properly cited.

https://doi.org/10.1017/jfm.2025.10918 Published online by Cambridge University Press

of an homogeneous fluid rotating at constant angular velocity owe their existence to the restorative nature of the Coriolis force (Greenspan 1968). When the container is harmonically forced by a global body force, such as libration or precession, inviscid eigenmodes of the container (Kelvin 1880) may be resonantly excited. These Kelvin modes have a discrete but dense spectrum within the inertial range, corresponding to frequencies less than twice the rotation rate of the container. In the inviscid limit, these modes are neutral, so to observe them in a viscous physical setting, they must be forced. Forcing at a frequency sufficiently close to the natural frequency of a Kelvin mode with small spatial gradients may resonantly excite the Kelvin mode. The forcing will also drive boundary layer separations at any inertial frequency resulting in shear layers consisting of inertial wavebeams in the container (Wood 1966; Baines 1967; McEwan 1970). The modes and wavebeams coexist, remain coherent, but nevertheless interact nonlinearly (Lopez & Marques 2014; Wu, Welfert & Lopez 2018). The resonated modes at very small forcing amplitudes are those whose spatio-temporal symmetries are consistent with the symmetries of the body force and, for larger amplitude forcing, other modes with different symmetries may be excited via triadic resonances (Lopez & Marques 2018; Wu, Welfert & Lopez 2020). Apart from varying the frequency and amplitude of the body force, differential forcing of the container introduces phase differences in the forcing which further highlights the intricate interactions between the resonated container modes and the forced wavebeams (Gutierrez-Castillo & Lopez 2017).

However, localised forcing of sufficiently small amplitude is not expected to resonate container modes and only to lead to the emission of wavebeams. Oser (1957) solved for the characteristics emitted from a small slender disk oscillating in the axial direction at the centre of a cylindrical container in the linear inviscid setting, and then Oser (1958) conducted laboratory experiments confirming that the conical shear layers emitted from the oscillating disk matched the characteristics of the associated linear inviscid wave equation. However, the experiments of Fultz (1959), also consisting of a small disk undergoing small amplitude oscillations along the rotation axis of the cylinder in which it was housed, suggested the excitation of the container modes when the forcing frequency corresponded to a low-order Kelvin mode. Those experiments used dye visualisation and a motor that was not able to keep the forcing frequency sufficiently constant, and so were not definitive.

The structure of the conical shear layers emitted from a small disk oscillating vertically in a rotating fluid-filled cylinder was more recently investigated by Messio *et al.* (2008) using particle image velocimetry (PIV). Their primary goal was to verify the linear inviscid inertial wave dispersion relation far from the disk, which they accomplished. An additional finding of their experiments was the presence of a vorticity patch with non-zero mean along the axis of the cylinder, suggesting the formation of a steadily rotating column of radius comparable to the radius of the disk. This column existed not only for forcing frequencies very much smaller than twice the rotation frequency ($\sigma \ll 2\Omega$), which would be consistent with Taylor columns (Taylor 1922, 1923), but essentially throughout the inertial range $\sigma \lesssim 2\Omega$. The axial vorticity in this column was found to be comparable to or larger than the axial vorticity in the conical shear layers emitted from the edges of the disk. This columnar feature could not be explained by the linear inviscid theory in an unbounded domain, which predicts no fluid motion outside the conical shear layers at finite forcing frequencies. The authors were concerned that the accuracy of their PIV measurements may not be sufficient to resolve the details of the central columnar vorticity patch, which they left open for future investigation.

In this paper, numerical simulations demonstrating the formation of a rotating column along the axis above and below an oscillating sphere are presented. We introduce a

https://doi.org/10.1017/jfm.2025.10918 Published online by Cambridge University Press

small localised perturbation in the centre of the cylinder by harmonically oscillating a small sphere of radius a in the axial direction with frequency $0 < \sigma < 2\Omega$ and axial displacement δ. Both the cylinder and the sphere rotate at angular rate Ω, as in some experiments (Oser 1958; Messio *et al.* 2008). Our main purpose is to explore the nature of the rotating column observed in the experiments of Messio *et al.* (2008) by a systematic exploration of parameter space. As they noted, laboratory-scale experiments face challenges in locally producing circularly polarised wavebeams that on the one hand are not impacted by their reflections on the container wall, and on the other hand are of sufficient strength to allow for an acceptable signal-to-noise ratio in their measurement. This leads to large forcing amplitudes, where nonlinear effects may not be negligible, and may be a major factor in the establishment of the columnar structure. Numerically, we are able to control the strength of the nonlinear terms to systematically study their contributions. Furthermore, by fully accounting for the rotating cylindrical container in which the sphere is oscillating, we are able to capture the reflections of the conical wavebeams and how the reflected wavebeams geometrically focus at the axis, as well as how selected Kelvin modes are resonantly excited.

2. Governing equations and the numerical scheme

A circular cylinder of radius R and height H is filled with a fluid of kinematic viscosity ν and rotates about its axis at a constant angular rate Ω. The ratio of the rotation time scale, $1/\Omega$, and the viscous time scale, H^2/ν, gives the Ekman number

$$E = \frac{\nu}{\Omega H^2}. \tag{2.1}$$

The rapid rotation regime corresponds to $E \ll 1$. A small sphere of radius a, co-rotating with the cylinder, is placed at the centre of the cylinder and is forced to harmonically oscillate in the axial direction with frequency σ and maximum axial displacement δ. A schematic of the flow system is shown in figure 1.

The system is non-dimensionalised using the sphere radius a as length scale and $1/\Omega$ as time scale. The non-dimensional Navier–Stokes equations in the rotating reference frame are

$$\partial \boldsymbol{u}/\partial t + (\boldsymbol{u}\cdot\boldsymbol{\nabla})\boldsymbol{u} = -\boldsymbol{\nabla} p - 2\boldsymbol{\Omega}\times\boldsymbol{u} + a_H^2 E\,\nabla^2\boldsymbol{u}, \quad \boldsymbol{\nabla}\cdot\boldsymbol{u} = 0, \tag{2.2}$$

where p is the reduced pressure incorporating the centrifugal term, $\boldsymbol{u}$ is the velocity in cylindrical coordinates $\boldsymbol{r} = (r, \theta, z) \in [0, a_R] \times [0, 2\pi] \times [-0.5a_H, 0.5a_H]$, the rotation axis is $\boldsymbol{\Omega} = (0, 0, 1)$, and the radial and axial aspect ratios are $a_R = R/a$ and $a_H = H/a$.

The velocity boundary conditions are no-slip, i.e. $\boldsymbol{u} = \boldsymbol{0}$ on the cylinder walls and the surface of the sphere, except for the axial component of $\boldsymbol{u}$ on the sphere, which is $2\omega\alpha\cos(2\omega t)$, where the non-dimensional axial displacement amplitude and frequency of the sphere are

$$\alpha = \delta/a \quad \text{and} \quad 2\omega = \sigma/\Omega. \tag{2.3}$$

For small α, the magnitude of the response flow velocity is proportional to α and it is convenient to introduce the normalisation $\boldsymbol{v} = \boldsymbol{u}/\alpha = (u, v, w)$ and $q = p/\alpha$. Equation (2.2) then becomes

$$\partial \boldsymbol{v}/\partial t + \alpha(\boldsymbol{v}\cdot\boldsymbol{\nabla})\boldsymbol{v} = -\boldsymbol{\nabla} q - 2\boldsymbol{\Omega}\times\boldsymbol{v} + a_H^2 E\nabla^2\boldsymbol{v}, \quad \boldsymbol{\nabla}\cdot\boldsymbol{v} = 0. \tag{2.4}$$

The axial component of $\boldsymbol{v}$ on the sphere is

$$w_s = 2\omega\cos(2\omega t) \tag{2.5}$$

https://doi.org/10.1017/jfm.2025.10918 Published online by Cambridge University Press

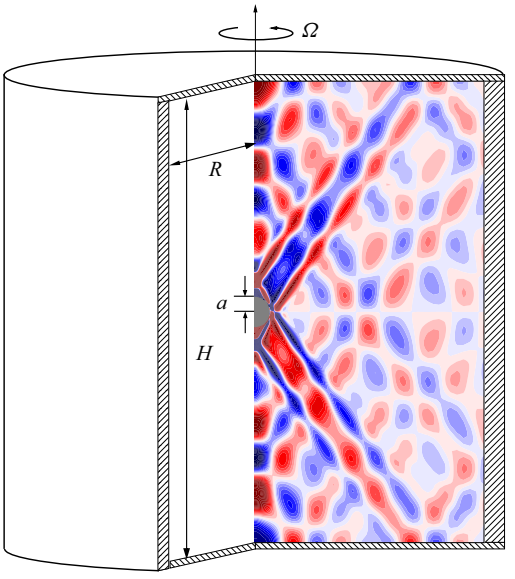

Figure 1. Schematic of the flow system. The inset shows a snapshot of the axially oscillating sphere and contours of axial vorticity ζ at $E = 1.77 \times 10^{-6}$, $\alpha = 0.476$ and $\omega = 0.54$, long after the flow transients have subsided.

and the axial location of the centre of the sphere is

$$z_s = \alpha \sin(2\omega t). \tag{2.6}$$

For sufficiently small α, the response flows are axisymmetric and synchronous with the forcing. With the sphere oscillating axially about the centre, the system (2.4)–(2.6) is also invariant to a half-period-flip spatio-temporal symmetry corresponding to a half-forcing-period advance in time composed with an odd reflection about the cylinder half-height; its action is

$$H_{sym} : [u, v, w](r, z, t) \mapsto [u, v, -w](r, -z, t + \tau/2), \tag{2.7}$$

where $\tau = \pi/\omega$ is the forcing period. In many experiments, the oscillating body is not placed in the centre of the container. For example, Messio *et al.* (2008) placed their oscillating disk on the axis at approximately $1/3$ depth, so that the system is not H_{sym} invariant. Furthermore, if the oscillating body is not centred on the axis, the response flows will be non-axisymmetric. For example, Messio *et al.* (2008, figures 4 and 5) show contributions from an azimuthal wavenumber $m = 1$, which they ascribe to 'a slight misalignment between the rotation axis and the cylinder symmetry axis'.

To diagnose the flows, we decompose the velocity into its linear, mean and nonlinear fluctuating parts,

$$\boldsymbol{v} = \boldsymbol{v}_0 + \overline{\boldsymbol{v}} + \widetilde{\boldsymbol{v}}, \tag{2.8}$$

where $\boldsymbol{v}_0$ is the linear solution with $\alpha = 0$ in (2.4); being linear, it has zero mean. The time-average of $\boldsymbol{v}$ is

$$\overline{\boldsymbol{v}} = \frac{1}{\tau} \int_0^\tau \boldsymbol{v} \, \mathrm{d}t. \tag{2.9}$$

The nonlinear fluctuations $\widetilde{\boldsymbol{v}}$ also have zero mean.

https://doi.org/10.1017/jfm.2025.10918 Published online by Cambridge University Press

The linear solution $\boldsymbol{v}_0$ is invariant to an additional odd reflection symmetry about the cylinder half-height since with $\alpha = 0$, the sphere is not displaced from the centre. The action of this reflection on $\boldsymbol{v}_0$ is

$$K_{sym} : [u_0, v_0, w_0](r, z, t) \mapsto [u_0, v_0, -w_0](r, -z, t). \tag{2.10}$$

The vorticity of an axisymmetric flow is

$$\boldsymbol{\nabla} \times \boldsymbol{v} = (\xi, \eta, \zeta) = (-1/r\ \partial rv/\partial z,\ \partial u/\partial z - \partial w/\partial r,\ 1/r\ \partial rv/\partial r). \tag{2.11}$$

The action of K_{sym} on the components of the vorticity of $\boldsymbol{v}_0$ is

$$K_{sym} : [\xi_0, \eta_0, \zeta_0](r, z, t) \mapsto [-\xi_0, -\eta_0, \zeta_0](r, -z, t). \tag{2.12}$$

For global measures of the response flows, we use the time-averaged enstrophy

$$\mathcal{E} = \frac{1}{\tau} \int_0^{\tau} \int_{-0.5a_H}^{0.5a_H} \int_0^{a_R} (\boldsymbol{\nabla} \times \boldsymbol{v})^2\, r\, \mathrm{d}r\, \mathrm{d}z\, \mathrm{d}t, \tag{2.13}$$

and the time-averaged kinetic energy

$$\mathcal{K} = \frac{1}{2\tau} \int_0^{\tau} \int_{-0.5a_H}^{0.5a_H} \int_0^{a_R} \boldsymbol{v}^2 r\, \mathrm{d}r\, \mathrm{d}z\, \mathrm{d}t, \tag{2.14}$$

The experimental results of Messio *et al.* (2008) are reported in terms of the axial component of vorticity, ζ. We will use this to present our results, as well as the azimuthal component of vorticity, η, as was done by Lopez & Marques (2014). These two components of vorticity are readily measured experimentally via PIV in planes orthogonal to the rotation axis (Messio *et al.* 2008) or in meridional planes (Subbotin 2020).

The system is governed by several non-dimensional parameters, and a comprehensive exploration of the parameter space is extremely expensive. All simulations presented here have $E = 1.77 \times 10^{-6}$, $a_R = 16$ and $a_H = 32$, similar to values used in the experiments of Messio *et al.* (2008), and consider variations in α and ω.

The governing equation (2.4), restricted to the axisymmetric subspace, is solved numerically using a fractional step scheme. The method has been implemented in many different scenarios and grid layouts (Verzicco & Orlandi 1996; Fadlun *et al.* 2000; Pacheco *et al.* 2011) and only a brief overview is given here. Spatial discretisation is via second-order-accurate finite-difference approximations on non-uniform meshes. Temporal evolution is via a third-order Runge–Kutta scheme which treats the nonlinear terms explicitly and the viscous terms implicitly. The stability limit due to the explicit treatment of the convective terms is CFL $< \sqrt{3}$, where CFL $= \delta t(|u_{i,j}|/\delta r_{i,j} + |v_{i,j}|/(2\pi r_{i,j}) + |w_{i,j}|/\delta z_{i,j})$ is the Courant–Friedrichs–Lewy number. The indexed quantities were averaged at the centre of each computational cell. The time step δt was selected from several test cases such that CFL < 1.5 was maintained overall. The formulation allows for variable δt throughout a simulation, but this was not implemented in the present study which is periodically forced. All results presented used $\delta t = 0.0001\tau$. A second-order in the space immersed boundary method is used to simulate the sphere, with the finite difference grid clustered at the sphere in the radial and axial directions. Tests were conducted with different grid sizes to verify grid independence of the results. Grid sizes up to $n_r \times n_z = 300 \times 600$ were tested. A grid resolution of $n_r \times n_z = 150 \times 300$ resulted in a maximum difference in velocities at various probe locations of less than 1 % compared with the finest grid, and this resolution has been used in the simulations presented in this paper. To reach synchronous states, approximately 3000 periods were required.

https://doi.org/10.1017/jfm.2025.10918 Published online by Cambridge University Press

3. Results

The response flows have been computed over the frequency range $0.050 \leq \omega \leq 0.995$ using steps in ω no greater than 0.005, with additional refinements in regions of rapid variation with ω. These have been computed over several decades in forcing amplitude, from $\alpha = 0.000476$ to 0.476. The largest α corresponds to that used in the experiments of Messio *et al.* (2008). We have also computed the linear response flow, corresponding to $\alpha = 0$. Figure 2(*a*) summarises the response flows in terms of their mean enstrophy $\mathcal{E}$, while figure 2(*b*) shows the same results in terms of $\mathcal{E}/\omega^2$ to better appreciate the responses at low ω. As anticipated when formulating (2.4), the responses are essentially independent of α, except for the largest α considered.

The response diagrams in figure 2 show a myriad of peaks and troughs throughout the inertial range. As noted by Lopez & Marques (2014), constructive or destructive interferences between inertial waves and their reflections, as well as with resonated cavity modes, contribute to peaks or troughs in the response diagram. It is likely that these peaks and troughs are associated with resonantly driven low-order Kelvin modes or retracing rays, but it is not a straight-forward exercise to establish this for a variety of reasons. Although the Ekman number, $E = 1.77 \times 10^{-6}$, is reasonably small by laboratory experimental standards (Le Bars *et al.* 2022), it is still large enough to cause viscous detuning effects that make correlating the peaks to the associated inviscid mode frequencies difficult (Wu *et al.* 2018). As for the retracing rays, if the sphere had zero radius and was treated as a point source, then simple ray tracing could be employed, as is done in other flows (Lopez & Marques 2014; Liu, Wang & Oberlack 2023), although even for those simpler cases, the finite thicknesses of boundary layers and inertial shear layers complicate the comparison between Navier–Stokes results and linear inviscid theory. Furthermore, the sphere of finite radius does not simply emit a double conical sheet from a point, but rather a complicated system of conical sheets from the critical latitudes on the sphere, where the characteristics associated with the linear dispersion relation are tangential to the sphere, as illustrated in figure 1. Similar double-cone structures result from vertical oscillations of a sphere in a linearly stratified medium (Appleby & Crighton 1987; Voisin 1991; Voisin, Ermanyuk & Flór 2011). The critical latitudes are symmetric in z and shift smoothly with variations in ω. For $0 < E \ll 1$, these sheets are emitted from the boundary layer on the oscillating sphere and tend to be viscously blurred. For $E = 1.77 \times 10^{-6}$, they are reasonably distinguishable. Another possible contribution to the peaks in the response is enhanced geometric focusing of various beams and reflected beams at the rotation axis $r = 0$.

Supplementary movie 1 available at https://doi.org/10.1017/jfm.2025.918 shows snapshots of the axial vorticity ζ at the zero phase of the sphere's oscillation at $\omega = 0.005i$ with $1 \leq i \leq 190$, for $\alpha = 0$ (the linear response), $\alpha = 0.0476$ (nonlinear, but synchronous) and $\alpha = 0.476$ (nonlinear and non-periodic). The linear $\alpha = 0$ responses most cleanly illustrate the structure of the nested conical shear layers, their blending with the boundary layers on the sphere and the complicated manner in which their reflections play out. When the reflections are near the corners where the cylinder sidewall meets the endwalls, there can be a splitting of the compound shear layer. The linear cases also illustrate the geometric focusing onto the axis due to curvature effects in the axisymmetric conical shear layers (Lopez & Marques 2014). This is akin to the focusing singularities found in the linear inviscid analysis of an oscillating sphere in a stratified medium (Appleby & Crighton 1987). This is also of the same nature as the geometric focusing that has been extensively studied for an oscillating torus in a rotating flow (Duran-Matute *et al.* 2013; Liu *et al.* 2022, 2023; Mohamed *et al.* 2024), resulting in enhanced axial vorticity locally where the sheets

https://doi.org/10.1017/jfm.2025.10918 Published online by Cambridge University Press

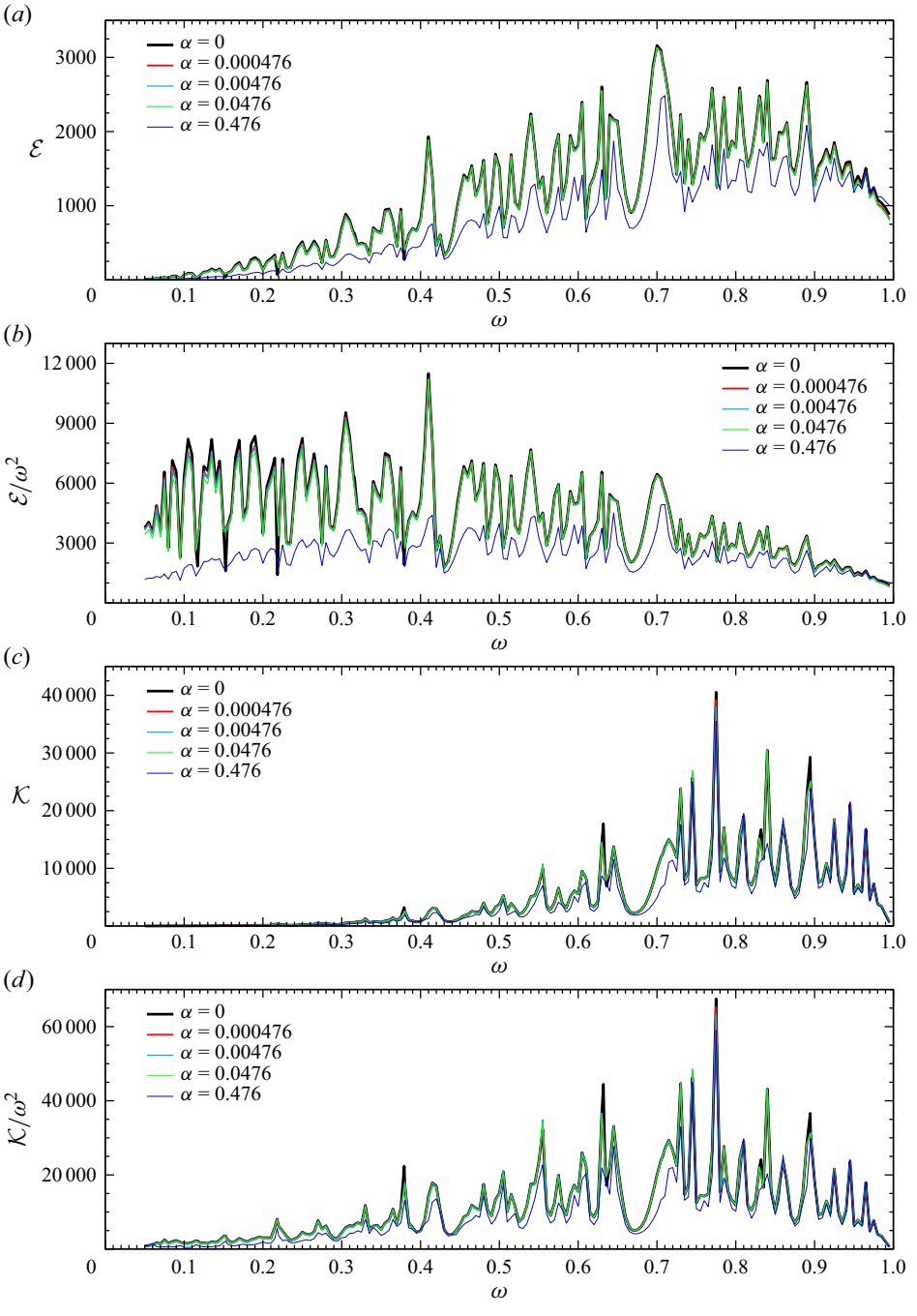

Figure 2. Variations with ω for α as indicated of (a) the mean enstrophy $\mathcal{E}$ and (c) the mean kinetic energy $\mathcal{K}$; panels (b) and (d) show the same data as in panels(a) and (c), but scaled with ω^2 to better appreciate the low-frequency response amplitudes. Supplementary movie 1 shows snapshots of the axial vorticity ζ at the zero phase of the sphere's oscillation at $\omega = 0.005i$ for $1 \leq i \leq 190$, for α as indicated.

https://doi.org/10.1017/jfm.2025.10918 Published online by Cambridge University Press

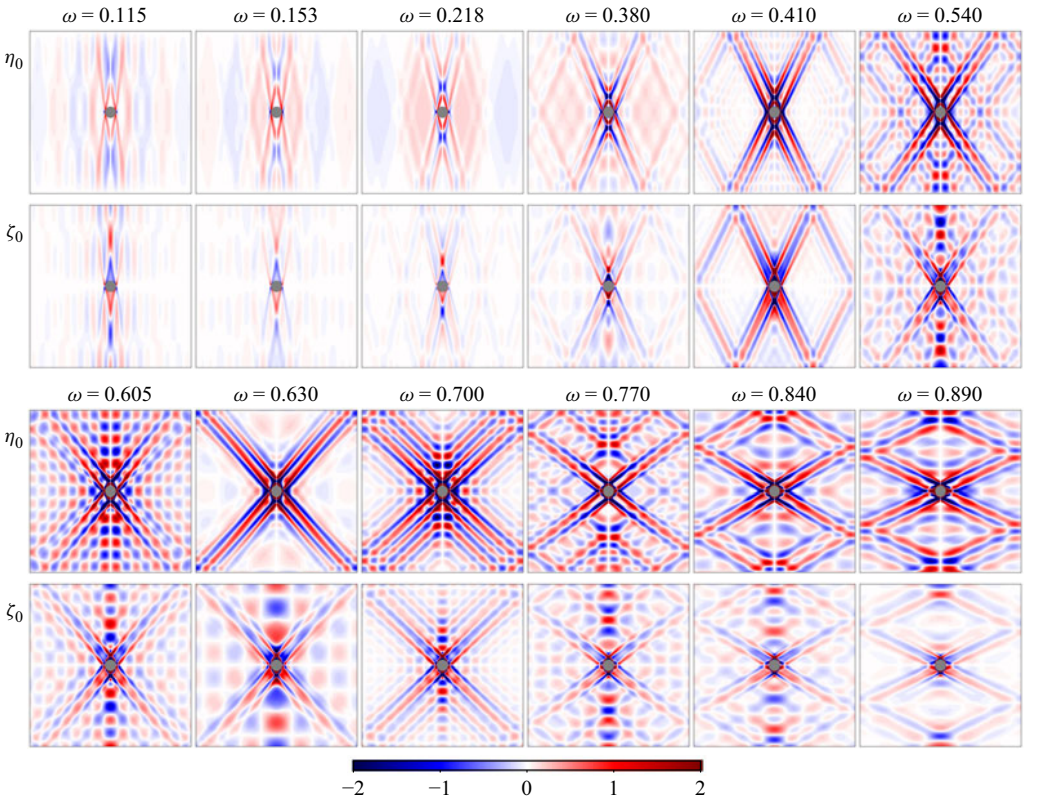

Figure 3. Snapshots of the azimuthal vorticity η_0 and axial vorticity ζ_0 at the zero phase of the forcing for $E = 1.77 \times 10^{-6}$, $\alpha = 0$ and ω as indicated. Supplementary movie 2 animates these over one forcing period.

focus. In the oscillating torus studies, attention was placed primarily on the initial focusing from the torus onto the axis and the fate of the conical sheets emitted to larger radii was not considered. With the oscillating sphere, the conical sheets emitted to smaller radii focus very close to the sphere and tend to be viscously blended with the boundary layer. The sheets emitted to larger radii are reflected on the sidewall and endwalls a number of times (depending on ω), and in the process, cross the axis at various z where they undergo the geometric focusing. The sign of the axial vorticity at emission from the critical latitudes changes every half-period as a consequence of the spatio-temporal symmetry H_{sym}, and the sheets emitted in the $+z$ direction have axial vorticity of the opposite sign to those emitted in the $-z$ direction. This all results in a sequence of regions of focused axial vorticity of alternating sign up and down the axis. The radial extents of these focused regions are of the order of the diameter of the sphere, smaller for small ω and larger for large ω.

3.1. *Linear responses*

We now look in detail at the linear responses, solutions to (2.4)–(2.6) with $\alpha = 0$. Figure 3 shows snapshots of η_0 and ζ_0, the azimuthal and axial components of vorticity of the linear responses ($\alpha = 0$), at the zero phase of the forcing for various ω. The four smallest values of ω correspond to the deepest troughs in the response diagram shown in figure 2(b). The rest correspond to peaks at higher ω. Supplementary movie 2 animates these over one forcing period. The expected conical shear layers emitted from the critical latitudes of the sphere are clearly evident, with cone angle consistent with the characteristic directions

https://doi.org/10.1017/jfm.2025.10918 Published online by Cambridge University Press

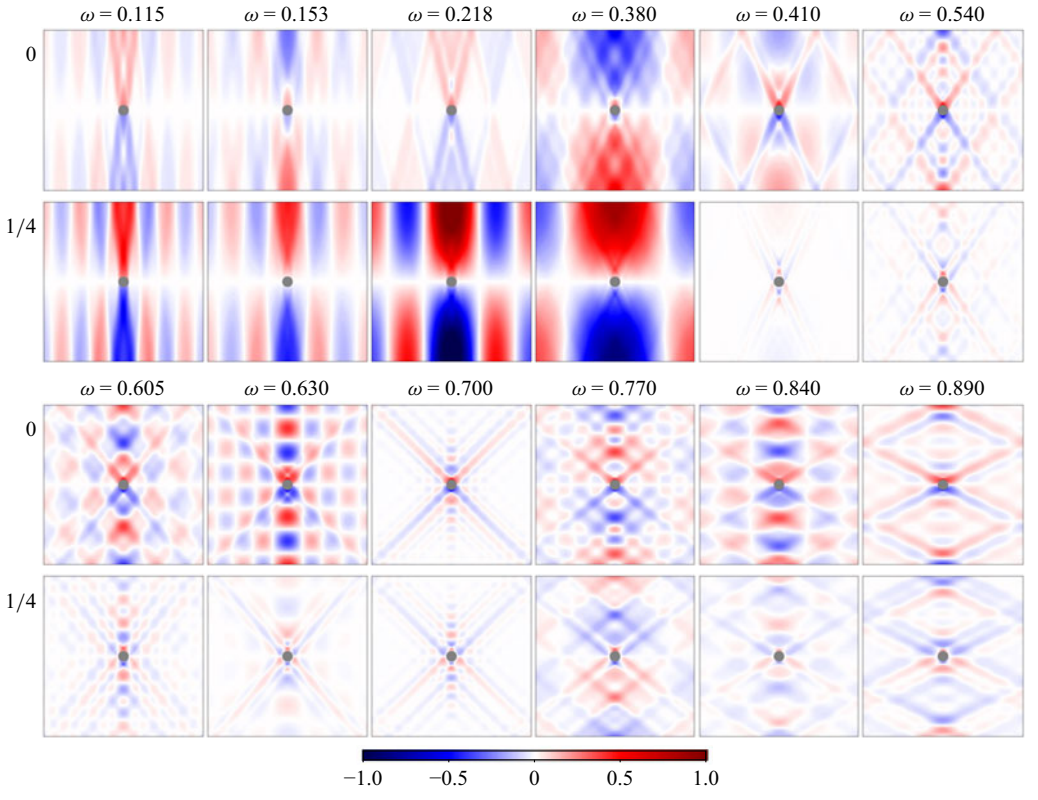

Figure 4. Snapshots of the pressure q_0 the zero and quarter phase of the forcing for $E = 1.77 \times 10^{-6}$, $\alpha = 0$ and ω as indicated. Supplementary movie 2 includes animations of q_0 over one forcing period.

from the linear inviscid dispersion relation. Their reflections on the walls of the cylinder and their geometric focusing as they approach the axis are also evident. At the small Ekman number considered, $E = 1.77 \times 10^{-6}$, their viscous attenuation is small enough that they survive several rounds of reflections. Also apparent are regular cellular structures that appear to be standing waves in supplementary movie 2. These have features associated with linear inviscid Kelvin modes at nearby frequencies (detuned by viscous effects).

Figure 4 shows snapshots of the pressure q_0 at the zero and quarter phase of the forcing corresponding to the response flows shown in figure 3. Looking at η_0, ζ_0 and q_0 helps to distinguish contributions from the forced conical shear layers, their enhancements due to retracing, and the resonant excitation of Kelvin modes. As the Ekman number is small, but not zero, there are inevitable viscous detuning effects. These detunings come in two flavours, one is that the inviscid Kelvin modes are resonated over a range of forcing frequencies near their inviscid natural frequency with the peak forcing frequency not exactly at the natural frequency, and the peak phase of the resonant response differs from the peak phase of the forcing depending on how close are the forcing and natural frequencies. These complicated detuning effects are illustrated in supplementary movie 2. A number of things stand out from the animations. For the four smallest ω, there is a very clear indication from the pressure that standing waves are being driven, with a peak response near, but not exactly, at the quarter phase. At the next value of $\omega = 0.410$, there is a hint of the standing wave at the lower $\omega = 0.380$, but the pressure is dominated by the shear layer structures which, at this ω, correspond to a retracing ray state. Here, the

https://doi.org/10.1017/jfm.2025.10918 Published online by Cambridge University Press

shear layers emitted from the sphere reflect on one endwall, then at the sidewall, followed by a reflection on the other endwall and then return to the sphere. There are other low-order retracing ray responses at $\omega = 0.700$ and 0.890, and a higher order retracing ray state at $\omega = 0.540$. The other responses at $\omega = 0.605$, 0.630 and 0.840 show standing wave responses with peaks near the zero phase of the forcing, whereas the response at $\omega = 0.770$ seems to show a standing wave response, but it is masked by the shear layer response. To better identify the standing wave responses, we next re-visit the linear inviscid Kelvin modes.

The Kelvin modes, $\boldsymbol{M}$, are the eigenmodes of the linear inviscid unforced system in solid-body rotation, corresponding to (2.4) with $E = \alpha = 0$ and no sphere. In a cylinder, separation of variables can be used to obtain these modes (Kelvin 1880). Marques & Lopez (2015, Appendix B) give explicit expressions for the pressure, velocity and vorticity fields to Kelvin modes with axial wavenumber n, radial wavenumber k and azimuthal wavenumber m. Here, we only consider the axisymmetric modes with $m = 0$, $\boldsymbol{M}_{n,k}$, and these are standing waves. The azimuthal and axial components of vorticity and the pressure of $\boldsymbol{M}_{n,k}$ are given by

$$\eta_{n,k}(r, z)\sin(2\sigma_{n,k}t) = \frac{n\pi\delta_k}{\Gamma\sigma_{n,k}a_R}J_1(r^*)\sin(n\pi z^*)\sin(2\sigma_{n,k}t), \tag{3.1}$$

$$\zeta_{n,k}(r, z)\cos(2\sigma_{n,k}t) = \delta_k J_0(r^*)\cos(n\pi z^*)\cos(2\sigma_{n,k}t), \tag{3.2}$$

$$q_{n,k}(r, z)\cos(2\sigma_{n,k}t) = \frac{2\delta_k\sigma_{n,k}^2\Gamma^2}{n\pi}J_0(r^*)\cos(n\pi z^*)\cos(2\sigma_{n,k}t), \tag{3.3}$$

where $\Gamma = H/R = a_H/a_R$, $r^* = \delta_k r/a_R$, $z^* = z/a_H + 1/2$, n and k are positive integers, δ_k is the kth zero of the Bessel function J_1, and the intrinsic half-frequency $\sigma_{n,k}$ is given by

$$\sigma_{n,k} = \left[1 + \left(\frac{\delta_k}{n\pi}\frac{a_H}{a_R}\right)^2\right]^{-1/2}. \tag{3.4}$$

The axisymmetric Kelvin modes $\boldsymbol{M}_{n,k}$ come in two flavours, depending on whether n is odd or even. For odd $n = 2i + 1$, the $\boldsymbol{M}_{n,k}$ have odd z-symmetry with

$$[\eta_{2i+1,k},\ \zeta_{2i+1,k},\ q_{2i+1,k}](r, z, t) \mapsto [-\eta_{2i+1,k},\ \zeta_{2i+1,k},\ q_{2i+1,k}](r, -z, t), \tag{3.5}$$

whereas for even $n = 2i$, they have even z-symmetry with

$$[\eta_{2i,k},\ \zeta_{2i,k},\ q_{2i+1,k}](r, z, t) \mapsto [\eta_{2i,k},\ -\zeta_{2i,k},\ -q_{2i+1,k}](r, -z, t). \tag{3.6}$$

Only the $\boldsymbol{M}_{n,k}$ with n odd are consistent with the K_{sym} symmetry of $\boldsymbol{v}_0$. The regular cellular standing wave structures of $\boldsymbol{v}_0$ shown in figure 3 for the selected frequencies ω, as well as in supplementary movie 2 over many ω, have the odd z-symmetry of the Kelvin modes $\boldsymbol{M}_{2i+1,k}$.

There is a general expectation that since the Kelvin modes with small wavenumbers are subjected to less viscous dissipation than those with large wavenumbers, imposing temporally harmonic forcing at a frequency sufficiently close to that of a Kelvin mode with small wavenumbers will resonate it (Aldridge & Toomre 1969). This is generally, but not universally, true when the forcing is of a global body force type, such as precession or differential rotation (Marques & Lopez 2015; Gutierrez-Castillo & Lopez 2017; Lopez & Marques 2018). With the localised forcing from the oscillating sphere, we find that not

https://doi.org/10.1017/jfm.2025.10918 Published online by Cambridge University Press

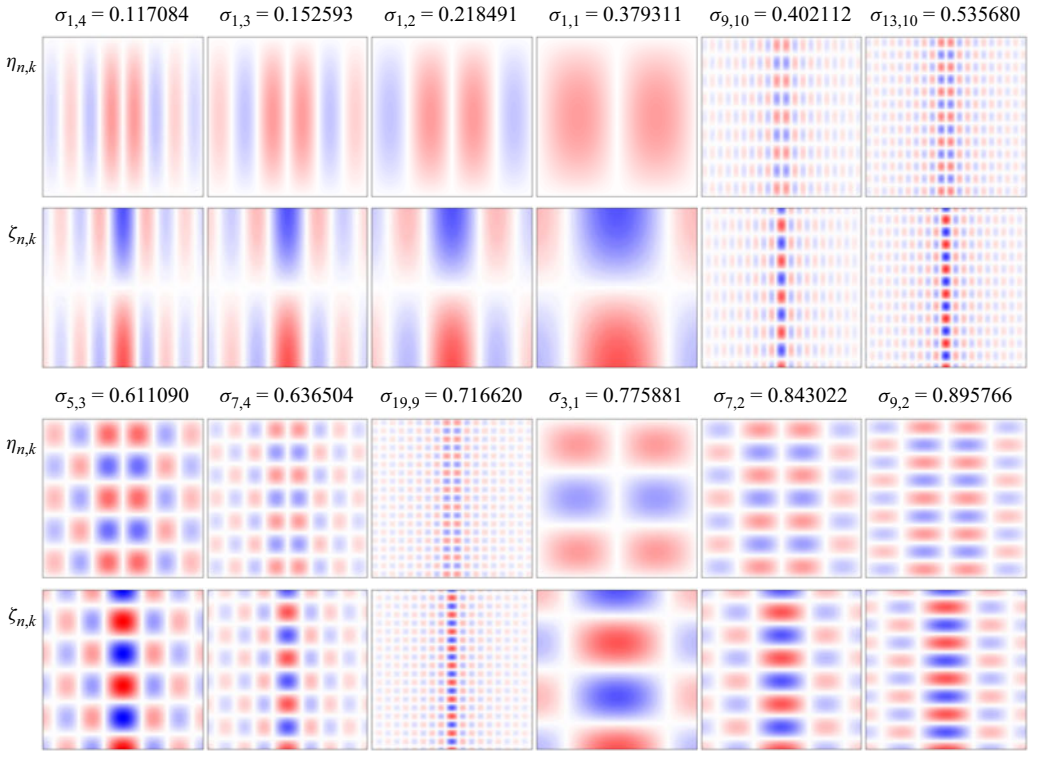

Figure 5. Spatial structure of the azimuthal vorticity $\eta_{n,k}$ and axial vorticity $\zeta_{n,k}$ of the axisymmetric Kelvin modes $\boldsymbol{M}_{n,k}$ at their intrinsic frequencies $\sigma_{n,k}$ (rounded to six figures) that are nearby the frequencies of the response flows shown in figure 3. Supplementary movie 3 animates these vorticity components of the Kelvin modes over one period.

only the forcing frequency, but also the spatial scale of the forcing plays a role in selecting the Kelvin mode that is resonated. Here, the diameter of the sphere dominates in setting the length scale of the conical shear layers and, together with how their reflections are distributed throughout the cylinder, play a role in selecting which Kelvin mode is resonated.

Figure 5 presents plots of $\eta_{n,k}$ and $\zeta_{n,k}$ of the axisymmetric Kelvin modes $\boldsymbol{M}_{n,k}$ at their intrinsic frequencies $\sigma_{n,k}$ (rounded to six figures) that are nearby the frequencies of the linear response flows $\boldsymbol{v}_0$ shown in figure 3, and appear to have the same axial and radial wavenumbers as the regular cellular standing wave structures of $\boldsymbol{v}_0$. The pressure $q_{n,k}$ is not plotted as it has the same spatial structure as $\zeta_{n,k}$. The Kelvin modes tend to have axial vorticity concentrated near the axis $r = 0$. This is due to the Kelvin modes having radial structures given by Bessel functions due to curvature effects, $1/r\,\partial/\partial r$, associated with the cylindrical container, and the Bessel function J_0 being maximal at the axis. Comparing figures 3 and 5, and supplementary movies 3 and 2, it is evident that the above-mentioned cases for which Kelvin modes are resonated are indeed so, and they have varying degrees of phase detuning depending on ω. For the retracing ray case at $\omega = 0.700$, there is a hint of cellular structures in the $\alpha = 0$ responses, especially in the pressure q_0, which correlates very well with $\boldsymbol{M}_{19,9}$ whose natural frequency is $\sigma_{19,9} = 0.716620$. The same is true of the retracing ray case at $\omega = 0.540$ and $\boldsymbol{M}_{13,10}$ with $\sigma_{13,10} = 0.535680$. These are Kelvin modes with large wavenumbers that are nevertheless resonated due to the widths of the retracing shear layers being comparable to the wavelengths of the modes.

https://doi.org/10.1017/jfm.2025.10918 Published online by Cambridge University Press

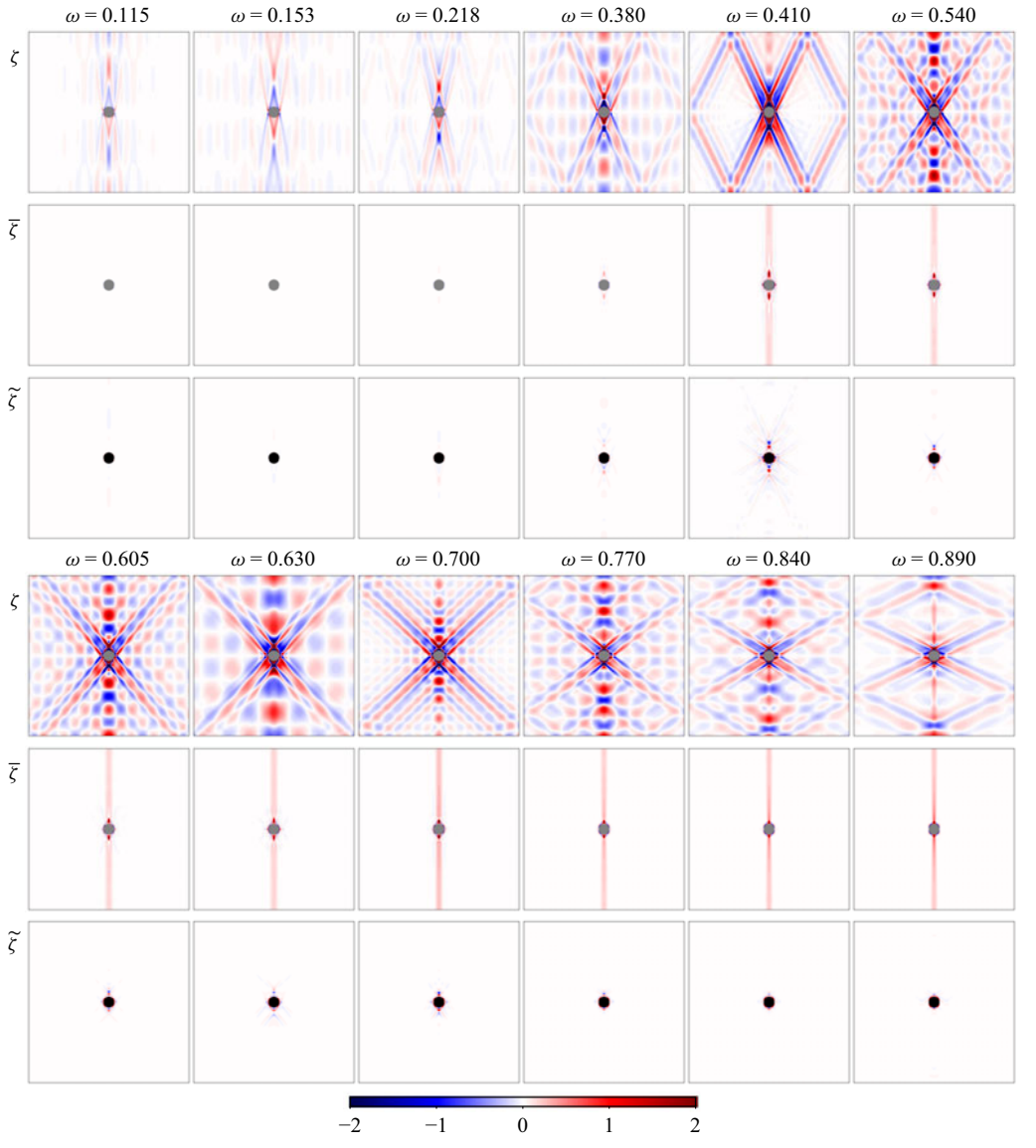

Figure 6. Snapshots of ζ, $\overline{\zeta}$ and $\widetilde{\zeta}$ for $E = 1.77 \times 10^{-6}$, $\alpha = 0.0476$ and ω as indicated. Supplementary movie 4 animates ζ over one forcing period.

However, the retracing ray case at $\omega = 0.410$ shows something different. From the vorticity components η_0 and ζ_0, there is a hint of $\boldsymbol{M}_{9,10}$ with $\sigma_{9,10} = 0.402112$ being resonated, but the pressure q_0 clearly indicates that $\boldsymbol{M}_{1,1}$ with $\sigma_{1,1} = 0.379311$ is weakly resonated.

3.2. *Nonlinear responses*

The response diagrams in figure 2 show that the mean enstrophy and kinetic energy, global measures of the flows, are essentially independent of α up to $\alpha \approx 0.0476$. We now consider in detail the responses at $\alpha = 0.0476$ for the same ω values considered for $\alpha = 0$ in the previous section. Figure 6 shows snapshots of the axial vorticity ζ for $\alpha = 0.0476$ at those values of ω, and supplementary movie 4 animates these over one period. At this α, the

https://doi.org/10.1017/jfm.2025.10918 Published online by Cambridge University Press

response flows are still periodic and synchronous with the forcing, but they are nonlinear. The figure also shows the time average $\overline{\zeta}$ and snapshots of the nonlinear fluctuations, obtained by subtracting the mean $\overline{\zeta}$ and the linear response ζ_0 (from the previous section) to obtain $\widetilde{\zeta} = \zeta - \overline{\zeta} - \zeta_0$, in accord with (2.8).

The mean $\overline{\zeta}$ is strong for $\omega \geq 0.380$, where shear layers emitted from the critical latitudes intersect at the axis $r = 0$, as well as where the other shear layers emitted from the critical latitudes intersect at the midplane $z = 0$. For lower ω, the response is too weak at this α (see figure 2). For the peak (rather than trough) responses ($\omega \geq 0.410$), there is an additional contribution to $\overline{\zeta}$ in the form of a columnar region of positive (cyclonic) $\overline{\zeta}$ centred on the axis, extending from the sphere to the top and bottom endwalls, and having a radial extent somewhat less than the radius of the sphere. This is akin to the mean columnar cyclonic vortex that emerges from the primary focusing of conical shear layers on the axis due to an axially oscillating torus in a rapidly rotating container (Duran-Matute *et al.* 2013). In this columnar region, away from the sphere and the intersections of the shear layers from the critical latitudes, $\overline{\zeta}$ is axially invariant, a so-called geostrophic zonal flow. This is along the lines of the more general result of Kafiabad, Vanneste & Young (2021), who state that geostrophic balance continues to hold in the presence of strong waves, but that this balance applies to the Lagrangian mean flow. In other words, even though the nonlinear flow with strong waves is not geostrophic, the mean flow is geostrophic. In their oceanographic setting with the strong waves flowing on a background current, a Lagrangian mean was needed. In our enclosed forced flow, taking the Eulerian temporal mean suffices. So, the columnar structure on the axis of the mean flow may be thought of as a Taylor column, steady and axially invariant, even though the flow from which it emerges is neither steady nor axially invariant (compare $\overline{\zeta}$ with ζ in figure 6 and supplementary movie 4).

Figure 6 also shows that the nonlinear fluctuations $\widetilde{\zeta}$ are particularly strong for the retracing ray cases at $\omega = 0.410$ and 0.700, and slightly weaker for $\omega = 0.540$. These cases have $\widetilde{\zeta}$ localised where the conical shear layers emitted from the critical latitudes first intersect on the axis and the midplane. For $\omega = 0.410$, in addition to this localised contribution, there are strong secondary conical shear layers emitted from the intersection points. These have cone angles consistent with the linear inviscid dispersion relation for twice the forcing frequency, $2\omega = 0.820$, which is still inertial. For $\omega = 0.54$ and 0.700, the second harmonic 2ω is no longer inertial and the nonlinear fluctuations $\widetilde{\zeta}$ are localised evanescent waves. The nonlinear fluctuations in the viscous boundary layer of the oscillating sphere are also localised to the boundary layer.

Increasing the forcing amplitude to $\alpha = 0.476$, essentially corresponding to that in the experiments of Messio *et al.* (2008), results in strongly nonlinear responses. Figure 7 shows the same quantities as figure 6, but for the higher $\alpha = 0.476$. A number of features stand out: the Taylor columns in $\overline{\zeta}$ are much more intense, roughly ten times as intense as the forcing amplitude is ten times larger; the boundary layer on the oscillating sphere tends to separate for ω corresponding to the most intense response flows; and the responses have broken the spatio-temporal symmetry H_{sym} and are no longer synchronous with the forcing. This is evident from the $\widetilde{\zeta}$ snapshots, but becomes immediately obvious from the animations of ζ in supplementary movie 5. A word of caution is warranted here, as the simulations have been restricted to the axisymmetric subspace. It is possible, and perhaps even probable, that the synchronous axisymmetric flow first loses stability by breaking axisymmetry, rather than breaking the H_{sym} symmetry first while remaining axisymmetric. Determining this is not a trivial exercise, which we leave open for now.

https://doi.org/10.1017/jfm.2025.10918 Published online by Cambridge University Press

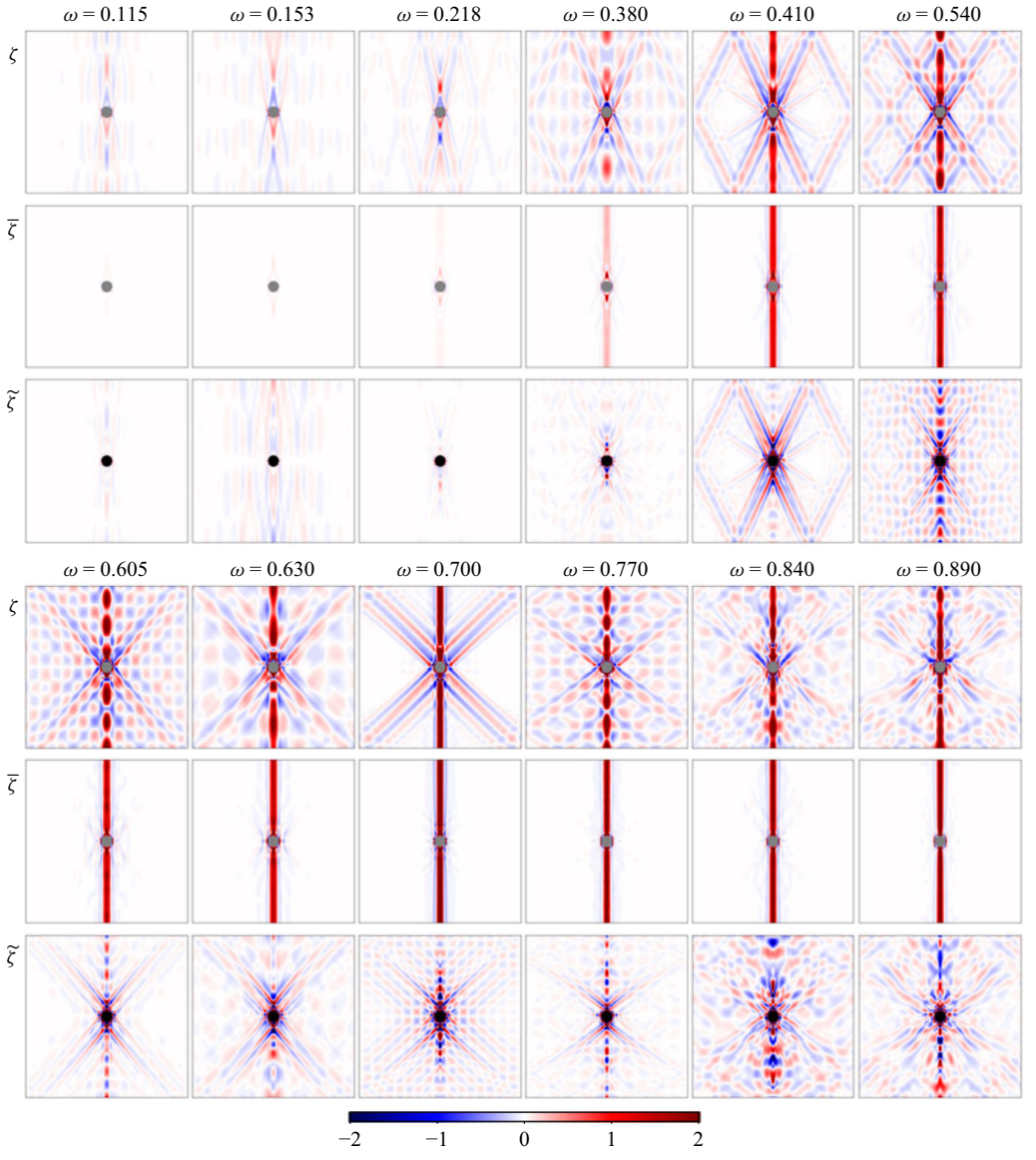

Figure 7. Snapshots of ζ, $\overline{\zeta}$ and $\widetilde{\zeta}$ for $E = 1.77 \times 10^{-6}$, $\alpha = 0.476$ and ω as indicated. Supplementary movie 5 animates ζ over one forcing period.

To quantify the transitions from linear through weakly nonlinear to nonlinear responses, figure 8 shows how the mean enstrophy, $\mathcal{E}(\boldsymbol{v})$, and the enstrophy of the mean flow, $\mathcal{E}(\overline{\boldsymbol{v}})$, vary with α for the 12 values of ω considered in figures 3, 6 and 7. In the weakly nonlinear regime, as noted in § 2, the non-dimensional velocity $\boldsymbol{u}$ is expected to scale linearly with α, and so the normalised velocity $\boldsymbol{v} = \boldsymbol{u}/\alpha$ should be independent of α, as should $\mathcal{E}(\boldsymbol{v})$. This is borne out in figure 8 (as well as in the response diagrams in figure 2), with $\mathcal{E}(\boldsymbol{v})$ only deviating away from its linear value at $\alpha = 0$ for the larger values of α considered. In the weakly nonlinear regime, the mean flow, $\overline{\boldsymbol{u}}$, would be expected to scale with α^2 and so $\overline{\boldsymbol{v}}$ should scale with α. With enstrophy being a squared quantity, this means that in the weakly nonlinear regime, $\mathcal{E}(\overline{\boldsymbol{v}})$ should scale with α^2. This is only observed to be so for

https://doi.org/10.1017/jfm.2025.10918 Published online by Cambridge University Press

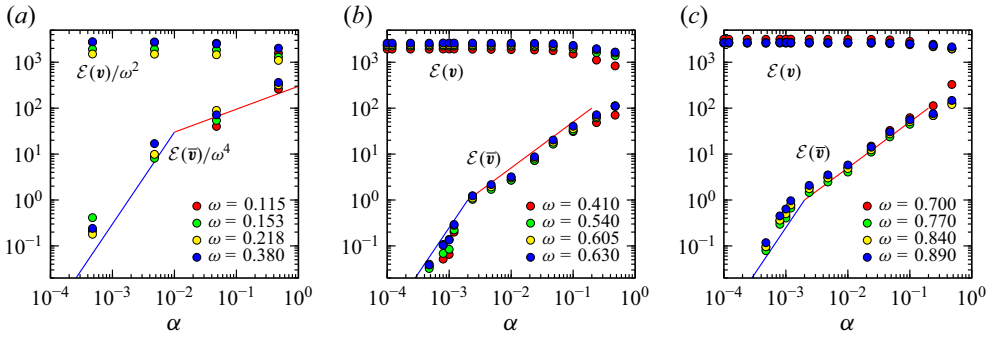

Figure 8. Variation of the mean enstrophy, $\mathcal{E}(\boldsymbol{v})$, and the enstrophy of the mean flow, $\mathcal{E}(\overline{\boldsymbol{v}})$, with α for ω as indicated. For the low-frequency cases shown in panel (*a*), $\mathcal{E}(\boldsymbol{v})$ is scaled by ω^2 and $\mathcal{E}(\overline{\boldsymbol{v}})$ by ω^4, while in panels (*b*) and (*c*) for the higher frequency cases, they are not scaled. In each plot, the blue line has slope 2 and the red line has slope 1, indicating a change from quasi-linear to nonlinear behaviour.

small $\alpha \lesssim 2 \times 10^{-3}$ (indicated by the blue lines of slope 2), while for larger α, $\mathcal{E}(\overline{\boldsymbol{v}})$ scales linearly with α (indicated by the red lines of slope 1), and there is a notable deviation in $\mathcal{E}(\boldsymbol{v})$ away from its linear value at these larger α. This change in the α-scaling of $\mathcal{E}(\overline{\boldsymbol{v}})$ indicates a transition from weakly nonlinear to nonlinear behaviour. This transition is at an α that is over 200 times smaller than that considered in the experiments of Messio *et al.* (2008).

4. Comparison with experiments of Messio *et al.* (2008)

So far, we have presented results involving a sphere oscillating about the centre of the rotating cylinder. One may wonder if the choice of a disk rather than a sphere and its placement on the axis closer to one endwall will have qualitative effects on the response flows. In this section, we compare the response flows due to a sphere and a disk of the same radius oscillating under the conditions of the experiments of Messio *et al.* (2008). Specifically, the experiments had Ekman number $E = 2.26 \times 10^{-6}$ (approximately 28 % larger than that used in the rest of the paper), $a_R = 16.6667$, $a_H = 40.0$ (compared with $a_r = 16$ and $a_H = 32$ used in the rest of the paper), and disk thickness to radius ratio of 0.238. The disk was oscillated about the axial location $z = 4a_H/21$ with amplitude $\alpha = 0.476$ and a range of frequencies. We shall compare the sphere and disk responses at the frequencies reported by Messio *et al.* (2008), corresponding to $\omega = 0.24$, 0.46, 0.66, 0.74 and 0.83. All the reported experimental results were from PIV measurements in a plane orthogonal to the rotation axis at $z = 5a_H/42$.

Figure 9 shows snapshots of the axial vorticity of the disk (top row) and sphere (bottom row) under the conditions specified in the previous paragraph. The grey horizontal line indicates the plane where PIV measurements were obtained in the experiments of Messio *et al.* (2008). All the responses are synchronous, for both the disk and the sphere, as can be seen from the animations of these responses over one forcing period in supplementary movie 6. In contrast, the $\alpha = 0.476$ responses from § 3 were not periodic for the larger ω; see the $\omega = 0.84$ and 0.89 cases in supplementary movie 5. While the experimental results are only reported for $\omega = 0.83$ and smaller, the 28 % larger Ekman number used also provides a corresponding larger viscous damping of the instability of the synchronous response. We can compare the response at the experimental ω with the responses for the sphere at the centre at the same ω by looking at the appropriate frames from supplementary movie 1. The most striking difference is the lack of H_{sym} in the off-centre responses.

https://doi.org/10.1017/jfm.2025.10918 Published online by Cambridge University Press

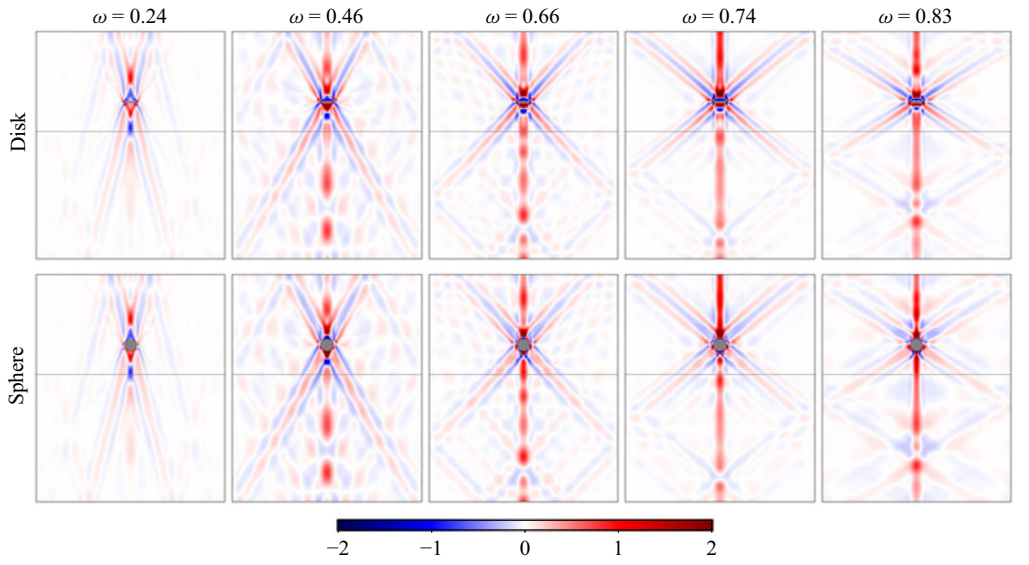

Figure 9. Snapshots of the axial vorticity ζ for $E = 2.26 \times 10^{-6}$, $a_R = 16.6667$, $a_H = 40.0$, $\alpha = 0.476$ and ω as indicated. The top row is for a disk and the bottom row for a sphere, both placed at the same axial location as in the experiments of Messio *et al.* (2008). The grey horizontal line indicates the plane where PIV measurements were obtained in those experiments. Supplementary movie 6 animates ζ over one forcing period.

This has two immediate consequences: (i) it affects the pattern of reflected conical shear layers – whether they retrace or not – and the conical shear layers emitted upwards have stronger reflections than those emitted downwards as they travel shorter distances before being reflected, further enhancing the asymmetry of the response; and (ii) since the axisymmetric Kelvin modes are either odd or even functions in the axial direction, z, having the disk or sphere oscillating about $z \neq 0$ makes directly resonating a Kelvin mode highly unlikely – there is no hint of a Kelvin mode being resonated in figure 9 or supplementary movie 6. All that being said, comparing the response flows with the on- and off-centre forcing in a small neighbourhood of the oscillating body (say, within a couple of body diameters), the pattern of emitted conical shear layers are very similar. Also, there are more differences between the oscillatory boundary layers of the disk and sphere in the off-centre case than between the sphere oscillatory boundary layers in the on- and off-centre cases.

Messio *et al.* (2008) also present radial profiles of the time-averaged and azimuthally averaged squared axial vorticity obtained from PIV measurements of the velocity components in a plane orthogonal to the axis at $z = 5a_H/42$ for the five frequencies shown in figure 9. One of the authors of that paper (Frédéric Moisy, private communication) very kindly provided us with those measurements, as well as additional measurements at small radii which were not published. We have reproduced these data in figure 10(a), where those data have been non-dimensionalised and normalised as we have done for our velocity $\boldsymbol{v}$, and taken the square-root to obtain a root-mean-squared (r.m.s.) measure, ζ_{rms}. The figure also includes the corresponding radial profiles of ζ_{rms} for the disk and sphere simulations shown in figure 9 and supplementary movie 6. We plotted the data as an r.m.s measure because the data for $r > 2$ are very small compared with those for $r < 2$ and would otherwise be swamped. The published experimental data (yellow symbols in figure 10) correspond to $r \gtrsim 2$, and these roughly agree with our simulations, both for the disk (blue lines) and the sphere (red lines). The agreements are probably not as good

https://doi.org/10.1017/jfm.2025.10918 Published online by Cambridge University Press

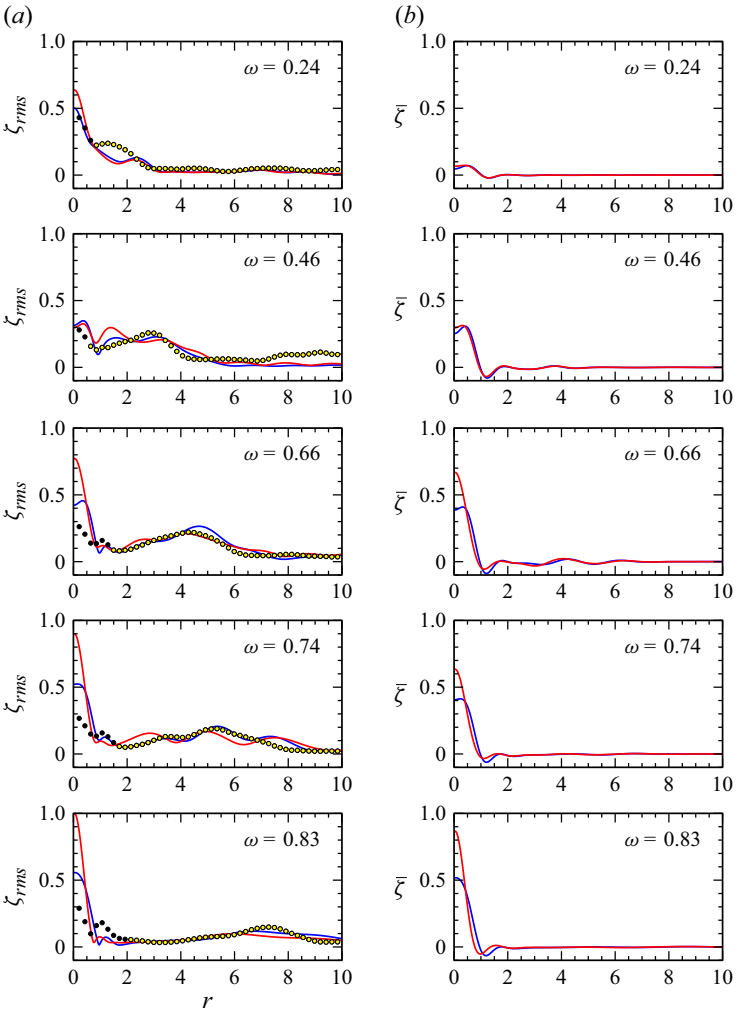

Figure 10. Radial profiles of ζ_{rms}, the square-root of the time average of the squared axial vorticity and of the time average of the axial vorticity $\overline{\zeta}$, at $z = 5a_H/42$ (the grey horizontal line shown in figure 9), for $E = 2.26 \times 10^{-6}$, $a_R = 16.6667$, $a_H = 40.0$, $\alpha = 0.476$ and ω as indicated. The yellow symbols are data from Messio *et al.* (2008), non-dimensionalised as in the rest of the present paper, the black symbols are data from the same experiments that were not published, but made available to us (Frédéric Moisy, private communication), the blue and red lines are our simulations using a disk and a sphere, respectively, under the same conditions.

as they should be due to the sparse temporal data used to obtain the experimental time averages. For each case, the experiments were phase averaged over 30 forcing periods, with each period containing between 6 and 40 velocity field measurements, depending on the forcing frequency. This was due to the constant sampling rate of the PIV set-up. As a consequence, the time averages were probably not taken over an integer number of forcing periods, and the number of time frames per period was small, especially for the higher frequencies. The unpublished experimental data (black symbols) do indicate larger responses for $r \lesssim 2$, but these are weaker than the simulation results, partially due to the sparse temporal sampling (fixed at 8 Hz).

The squared vorticity data in figure 10(*a*) do not inform on whether the central vortex at $r \lesssim 1$ is cyclonic (positive mean ζ) or anticyclonic (negative mean ζ). The radial profiles

https://doi.org/10.1017/jfm.2025.10918 Published online by Cambridge University Press

in figure 10(*b*) are of the time-averaged axial vorticity, $\overline{\zeta}$, corresponding to the same simulations as in figure 10(*a*). These quantify what is seen in figure 9 and supplementary movie 6: for both the disk and the sphere, the mean central vortex is strongly cyclonic from the axis to a little past the edge of the oscillating body, it is shrouded by a narrow weaker anticyclonic sheath, and then remains essentially at zero for larger radii except where conical shear layers (either primary or reflected) intercept the plane. This is in contrast to what is reported from the experiments. Messio *et al.* (2008, figures 4 and 5) show negative axial vorticity about the axis: 'this vorticity patch at the centre also shows a significant non-zero mean (anticyclonic vorticity), as can be seen in figure 5'. However, they also state that 'the background rotation is clockwise'. The apparent clockwise background rotation is a consequence of their PIV camera looking up from below; the horizontal velocity vectors closest to the axis shown in their figure 4 also show clockwise rotation, which corresponds to positive (cyclonic) axial vorticity, although their colourbar labels it as negative.

5. Summary and conclusions

By means of numerical simulations, the Navier–Stokes equations with no-slip boundary conditions, a comprehensive study of the response flows in a rapidly rotating fully enclosed cylinder driven by a small sphere oscillating harmonically at its centre has been undertaken. Such a localised forcing in a rotating medium has been used in the past to interrogate localised inertial waves experimentally, but attempts to reconcile observations with the available theory that relies on a far-field approximation and a neglect of the reflected inertial waves from the walls of the container were challenging. Further complicating the reconciliation between experiments and theory is that the theory is linear, whereas the experimental observations needed to be nonlinear to have an acceptable signal-to-noise ratio for their measurements.

Numerically, we have considered the full inertial forcing frequency spectrum and forcing amplitudes ranging from vanishingly small, to access the purely linear responses, to amplitudes just large enough that the synchronised symmetric response flows at lower forcing amplitudes lose stability. The simulations have been done in a parameter regime comparable to that in the experiments of Messio *et al.* (2008). The primary response is in the form of compound oscillatory conical shear layers emitted from the viscous boundary layer on the sphere. Where these are emitted corresponds very well with the critical latitudes on the sphere where the characteristic directions from the hyperbolic system obtained from linear inviscid theory are tangential to the sphere, and the conical shear layers follow those characteristic directions. This aspect of the response flows is in agreement with the experimental observations. Not detected in the experiments were resonated inertial cylinder modes, the Kelvin modes. The linear and the nonlinear simulations found that at forcing frequencies close to the natural frequencies of some Kelvin modes, those modes were resonantly excited. As is to be expected, the modes resonated had symmetries compatible with the symmetry of the forced system. However, the modes have a dense spectrum and there are many potential candidates to be resonated, given the viscous effects associated with the small but finite Ekman number of the flows. In some cases, particularly for the lower forcing frequencies, the lowest order modes (in this case, those with vertical wavenumber equal to one) were resonated. This is compatible with the fact that the lower order modes are subjected to less viscous damping. However, for higher frequency forcing, higher order modes were resonated instead of lower order modes with comparable natural frequencies. We surmise that these higher order modes were preferentially resonated due to their spatial wavelengths being comparable to the diameter of the sphere. So, the localised forcing does have a direct bearing on the form

https://doi.org/10.1017/jfm.2025.10918 Published online by Cambridge University Press

of the response, but the global nature of the container is ever present, both in the form of resonated container modes as well as impacts from reflected inertial shear layers, particularly at forcing frequencies where the reflected shear layers retrace back to the sphere after a small number of reflections.

One of our initial motivations for undertaking this study was to reconcile the experimentally observed columnar vortex patch, with a significant non-zero mean, between the oscillating central body and the top and bottom endwalls of the container. We show that this is indeed a part of the nonlinear response and that it amounts to a Taylor column associated with the time-averaged flow, with its intensity proportional to the forcing amplitude squared in the weakly nonlinear regime and linearly proportional to the forcing amplitude for larger forcing amplitude where the response flow is nonlinear, but still synchronous.

Supplementary movies. Supplementary movies are available at https://doi.org/10.1017/jfm.2025.918.

Acknowledgement. The authors thank ASU Research Computing for use of their facilities.

Declaration of interests. The authors report no conflict of interest. NAVAIR Public Release 2025-0295. Distribution A – 'Approved for public release; distribution is unlimited.'

References

ALDRIDGE, K.D. & TOOMRE, A. 1969 Axisymmetric inertial oscillations of a fluid in a rotating spherical container. *J. Fluid Mech.* **37**, 307–323.

APPLEBY, J.C. & CRIGHTON, D.G. 1987 Internal gravity waves generated by oscillations of a sphere. *J. Fluid Mech.* **183**, 439–450.

BAINES, P.G. 1967 Forced oscillations of an enclosed rotating fluid. *J. Fluid Mech.* **30**, 533–546.

DURAN-MATUTE, M., FLÓR, J.-B., GODEFERD, F.S. & JAUSE-LABERT, C. 2013 Turbulence and columnar vortex formation through inertial-wave focusing. *Phys. Rev. E* **87**, 041001(R).

FADLUN, E.A., VERZICCO, R., ORLANDI, P. & MOHD-YUSOF, J. 2000 Combined immersed-boundary finite-difference methods for three-dimensional complex flow simulations. *J. Comput. Phys.* **161**, 35–60.

FULTZ, D. 1959 A note on overstability and the elastoid-inertia oscillations of Kelvin, Soldberg, and Bjerknes. *J. Meteorol.* **16**, 199–208.

GREENSPAN, H.P. 1968 *The Theory of Rotating Fluids*. Cambridge University Press.

GUTIERREZ-CASTILLO, P. & LOPEZ, J.M. 2017 Nonlinear mode interactions in a counter-rotating split-cylinder flow. *J. Fluid Mech.* **816**, 719–745.

KAFIABAD, H.A., VANNESTE, J. & YOUNG, W.R. 2021 Wave-averaged balance: a simple example. *J. Fluid Mech.* **911**, R1.

KELVIN, L. 1880 Vibrations of a columnar vortex. *Phil. Mag.* **10**, 155–168.

LE BARS, M., BARIK, A., BURMANN, F., LATHROP, D.P., NOIR, J., SCHAEFFER, N. & TRIANA, S.A. 2022 Fluid dynamics experiments for planetary interiors. *Surv. Geophys.* **43**, 229–261.

LIU, J., OBERLACK, M., WANG, Y., DELACHE, A. & GODEFERD, F.S. 2022 Focusing of inertial waves by a vertically annular forcing. *Phys. Fluids* **34**, 086601.

LIU, J., WANG, Y. & OBERLACK, M. 2023 Focusing of weakly nonlinear inertial waves by a vertically oscillating annular forcing. *Phys. Fluids* **35**, 116606.

LOPEZ, J.M. & MARQUES, F. 2014 Rapidly rotating cylinder flow with an oscillating sidewall. *Phys. Rev. E* **89**, 013013.

LOPEZ, J.M. & MARQUES, F. 2018 Rapidly rotating precessing cylinder flows: forced triadic resonances. *J. Fluid Mech.* **839**, 239–270.

MARQUES, F. & LOPEZ, J.M. 2015 Precession of a rapidly rotating cylinder flow: traverse through resonance. *J. Fluid Mech.* **782**, 63–98.

MCEWAN, A.D. 1970 Inertial oscillations in a rotating fluid cylinder. *J. Fluid Mech.* **40**, 603–640.

MESSIO, L., MORIZE, C., RABAUD, M. & MOISY, F. 2008 Experimental observation using particle image velocimetry of inertial waves in a rotating fluid. *Exp. Fluids* **44**, 519–528.

MOHAMED, A., DELACHE, A., GODEFERD, F.S., LIU, J., OBERLACK, M. & WANG, Y. 2024 Maximization of inertial waves focusing in linear and nonlinear regimes. *Phys. Rev. Fluids* **9**, 094605.

OSER, H. 1957 Erzwungene Schwinggungen in rotierenden Flüssigkeiten. *Arch. Rat. Mech. Anal.* **1**, 81–96.

https://doi.org/10.1017/jfm.2025.10918 Published online by Cambridge University Press

OSER, H. 1958 Experimentelle Untersuchung über harmonische Schwingungen in rotierenden Flüssigkeiten. *Z. Angew. Math. Mech.* **38**, 386–391.

PACHECO, J.R., RUIZ-ANGULO, A., ZENIT, R. & VERZICCO, R. 2011 Fluid velocity fluctuations in a collision of a sphere with a wall. *Phys. Fluids* **23**, 063301.

SUBBOTIN, S. 2020 Steady circulation induced by inertial modes in a librating cylinder. *Phys. Rev. Fluids* **5**, 014804.

TAYLOR, G.I. 1922 The motion of a sphere in a rotating liquid. *Proc. R. Soc. Lond. A* **102**, 180–189.

TAYLOR, G.I. 1923 Experiments on the motion of solid bodies in rotating fluids. *Proc. R. Soc. Lond. A* **104**, 213–218.

VERZICCO, R. & ORLANDI, P. 1996 A finite-difference scheme for three-dimensional incompressible flows in cylindrical coordinates. *J. Comput. Phys.* **123**, 402–414.

VOISIN, B. 1991 Internal wave generation in uniformly stratified fluids. Part 1. Green's function and point sources. *J. Fluid Mech.* **231**, 439–480.

VOISIN, B., ERMANYUK, E.V. & FLÓR, J.-B. 2011 Internal wave generation by oscillation of a sphere, with application to internal tides. *J. Fluid Mech.* **666**, 308–357.

WOOD, W.W. 1966 An oscillatory disturbance of rigidly rotating fluid. *Proc. R. Soc. Lond. A* **293**, 181–212.

WU, K., WELFERT, B.D. & LOPEZ, J.M. 2018 Librational forcing of a rapidly rotating fluid-filled cube. *J. Fluid Mech.* **842**, 469–494.

WU, K., WELFERT, B.D. & LOPEZ, J.M. 2020 Precessing cube: resonant excitation of modes and triadic resonance. *J. Fluid Mech.* **887**, A6.

https://doi.org/10.1017/jfm.2025.10918 Published online by Cambridge University Press